


Monitoring the sedimentary budget and dislocated boulders in western Greece – results since 2008

DIRK HOFFMEISTER , CONSTANZE CURDT and GEORG BARETH
GIS and Remote Sensing Research Group, Institute of Geography, University of Cologne, Cologne,
50923, Germany (E-mail: dirk.hoffmeister@uni-koeln.de)

Associate Editor – César Andrade

ABSTRACT

Dislocated boulders are one sign of high-energy wave impacts on coasts. These high-energy impacts, caused by severe storms or tsunamis, can trigger initial cracking and transport of boulders. Monitoring of these boulders, as well as the associated coastal sites is important in distinguishing between gradual coastal processes and high-energy events. Western Greece is a seismically active area, where tsunamis and high-energetic storms might occur and such past events are documented by historic and geoscientific research, making it an ideal location for monitoring dislocated boulders. Since 2008, monitoring of eight different coastal sites in this region was conducted by terrestrial laser scanning and photogrammetric approaches, with low-cost unmanned aerial vehicles. The re-use of similar surveying points in following years, allowed highly accurate monitoring. Point clouds derived from these methods were evaluated for change detection by point cloud comparisons. The data were also used to establish accurate three-dimensional models of dislocated boulders ($n = 70$). The determined boulder volumes of these accurate three-dimensional models were incorporated in wave transport equations and wave decay curves, and compared with monitoring results. A comprehensive overview of dislocated boulders in western Greece is presented. Three-dimensional boulder reconstruction is compared to an approach which uses a tape-based measuring of boulder axes, with the tape-based measurement showing a mean overestimation of mass by 32%. Accurate monitoring over time by both methods, is achieved by using fixed networks of reference points. Changes for each site over time, detected by direct point cloud comparisons, are fit to the possible inundation calculated by wave decay curves based on computed minimum wave heights for boulder transport. Both storm and tsunami waves may have initiated movement from the cliff edge and further transport is also possible. However, boulders showed no further movement from their current position in the area for the time period of this study.

Keywords Beaches, boulders, monitoring, terrestrial laser scanning, UAV.

INTRODUCTION

Dislocated boulders are one sign of high-energy wave impact on coastlines; and their presence has been reported from many other coastlines worldwide (Scheffers & Kelletat, 2003). They are

the subject of a controversial debate over whether their origin is related to tsunamis or to powerful storms, which in turn has important implications for coastal hazard assessment (Nott, 2003a; Spiske *et al.*, 2008; Goto *et al.*, 2010a; Paris *et al.*, 2011; Cox *et al.*, 2018a).

Additionally, these boulders can be used to approximate the age of the event (tsunami or storm) through mortality age dating of adherent marine organisms, such as corals, mussels and molluscs (Terry *et al.*, 2013). Other dating methods have been tested in the past to allow for more robust and accurate age estimations (Rixhon *et al.*, 2017).

Several hydrodynamic wave transport equations have been developed, providing approximations of minimal wave heights and velocities required to move boulders during extreme events (Nott, 2003a; Benner *et al.*, 2010; Lorang, 2011; Nandasena *et al.*, 2011; Engel & May, 2012). All wave transport equations estimate the forces acting on a boulder impacted by a wave. The most commonly used or altered equations, as first presented by Nott (2003b), consider three different pre-transport settings. These are: (i) a subaerial setting; (ii) a submerged setting; or (iii) a joint-bounded setting. Imamura *et al.* (2008), introduced a more sophisticated modelling approach, achieved through experimentation with cubic and rectangular shaped boulder models in a water channel. Rolling and saltation were determined to be the major transport mechanisms; however, flume-based experiments indicate that the complexity of boulder movement is much greater (Oetjen *et al.*, 2017).

For the determination of geomorphometric parameters of dislocated boulders, measurements of the three main axes are usually taken by measuring tape during field surveys (Goto *et al.*, 2010b; Paris *et al.*, 2010; Switzer & Burston, 2010; Shah-hosseini *et al.*, 2011). Manual roundness measurements can also be used to determine the organization of boulder fields and show a grade of reworking by movement (Cox *et al.*, 2018b); or a flatness index can be established to show boulder distribution (Lau *et al.*, 2018). However, between studies, methods for measuring boulder axes differ. Pignatelli *et al.* (2009) for example, used the *a*-axis and *b*-axis as major and medium axes, whereas others defined boulder axes by their orientation to the coastline (Noormets *et al.*, 2004; Benner *et al.*, 2010; Etienne *et al.*, 2011).

Some approaches of wave transport equations rely on 'mass' as a direct input parameter (Noormets *et al.*, 2004; Benner *et al.*, 2010; Etienne *et al.*, 2011; Engel & May, 2012) which is a function of volume and density. Thus, some authors take into consideration an approximation of the shape of each boulder to achieve better mass estimations based on measurement of the

boulder's axes (Etienne *et al.*, 2011). Spiske *et al.* (2008) actually weighed smaller boulders and compared their data to measurements of a laser profiler and the simplified method of multiplying the axes. Further considerable inaccuracies concerning the determination of the mass of each boulder, occur from rough approximations of rock density values. The calculation of reliable results to be used in wave transport equations requires more accurate input parameters. The latter can be conducted for instance by RTK-positioning (real-time kinematic positioning) (Engel & May, 2012), stereo-photogrammetric approaches (Gienko & Terry, 2014; Rovere *et al.*, 2017) or terrestrial laser scanning (TLS) (Scicchitano *et al.*, 2012; Hoffmann *et al.*, 2013). Hoffmeister *et al.* (2014) presented a dataset of 16 boulders from 2008 in western Greece and showed an average overestimation of boulder mass of 67% based on multiplication of the axes of boulders in contrast to the more accurate three-dimensional reconstruction and volume calculation. Following this, several authors applied correction factors to their axes-based calculations (Shah-Hosseini *et al.*, 2016).

Monitoring of dislocated boulders and their surrounding areas can be used to determine further displacements, as well as to discriminate between gradual coastal changes. A TLS-based monitoring approach conducted between 2009 and 2011 (Hoffmeister *et al.*, 2013) in western Greece; shows the occurrence of severe storms, as well as a high amount of seismic activity which may act as a possible trigger for tsunamis. The results, collected from the eight sites also presented here, showed annual reworking of the beach which resulted in redistribution of gravel and jetsam on slightly elevated areas but no detectable change/redistribution on cliff-top platforms.

In this contribution, new results from monitoring of dislocated boulders in western Greece, beginning in 2008, are presented. Monitoring began in 2008; and in 2014, low-cost unmanned aerial vehicles (UAV) were tested and have been used ever since. New data from a boulder site at Cape Schinou, Cefalonia Island, has also been added. The entire dataset from western Greece now consists of parameters for 70 dislocated boulders. In addition to previous publications (Hoffmeister *et al.*, 2013, 2014), this contribution focuses on different wave decay curves for each site, which were computed and related to results of wave transport equations relying on boulder mass (Engel & May, 2012). The mass is

accurately derived by the reconstruction of 3D models of each boulder, based on TLS-data and corresponding density values. Results of monitoring in this study fit estimated maximum wave inundations and show that all boulders were not further moved.

STUDY AREA

Western Greece

Starting in 2008, field campaigns were carried out at selected coastal sites in western Greece, along the coastline of the eastern Ionian Sea (Vött *et al.*, 2010; Hoffmeister *et al.*, 2013, 2014). Western Greece is directly adjacent to the Hellenic Trench, a major tectonic zone in the eastern Mediterranean (Louvari *et al.*, 1999; Clément *et al.*, 2000; Sachpazi *et al.*, 2000). Thus, the region is characterized by a high seismic and tsunami hazard risk (Papazachos & Dimitriu, 1991). In fact, numerous historical accounts (Soloviev *et al.*, 2000), as well as detailed sedimentary studies indicate repeated tsunami landfall in western Greece (Scheffers *et al.*, 2008; Vött *et al.*, 2010; May *et al.*, 2012). However, Marriner *et al.* (2017), using statistical analysis, suggested that repeated cycles of strong storms could be an alternative cause for boulder movement. Likewise, winter storms in this region may also have considerable impact on the coastal configuration, as reported for the Italian

coasts of the Ionian Sea (Mastronuzzi & Sansò, 2004; Barbano *et al.*, 2010).

At several sites in the Mediterranean, wave transport equations set up by Nott (2003b) are widely used and partly refined wave transport equations have also been used in the past. Scicchitano *et al.* (2007) obtained minimum tsunami wave heights of 2 to 3 m for the Maddalena Peninsula, south-east Sicily. For the Algerian coast, larger boulders were reported by Maouche *et al.* (2009) and minimum tsunami wave heights of *ca* 2 m were calculated. In Mastronuzzi & Sansò (2004), boulders from southern Apulia, Italy, requiring calculated tsunami wave heights of 1.5 m were described. Revised equations of Nott (2003b), were applied by Barbano *et al.* (2010) in Sicily and by Pignatelli *et al.* (2009) in southern Italy, yielding minimum tsunami wave heights of around 1 m and storm wave heights of *ca* 10 m. Similar results were found for the north-east Aegean Sea (Vacchi *et al.*, 2012).

Individual site descriptions

In this study, eight coastal sites (Fig. 1), differing in location, configuration and type, were repeatedly surveyed. For a comparison of the determined annual changes, data from two buoys of the Poseidon network (HCMR, 2018) were used (Fig. 1). Examples of dislocated boulders from selected sites of this study are shown in Fig. 2A to D. It is generally assumed, for all areas, that the distance between the



Fig. 1. (A) Location of western Greece in the east Mediterranean. (B) Map of all research sites (white dots) in western Greece, as well as buoy locations (white 'x'). The map is based on MODIS satellite imagery (2009). (C) The south-west part of Cefalonia Island, indicating study sites. This map is based on Landsat 7 (2009).

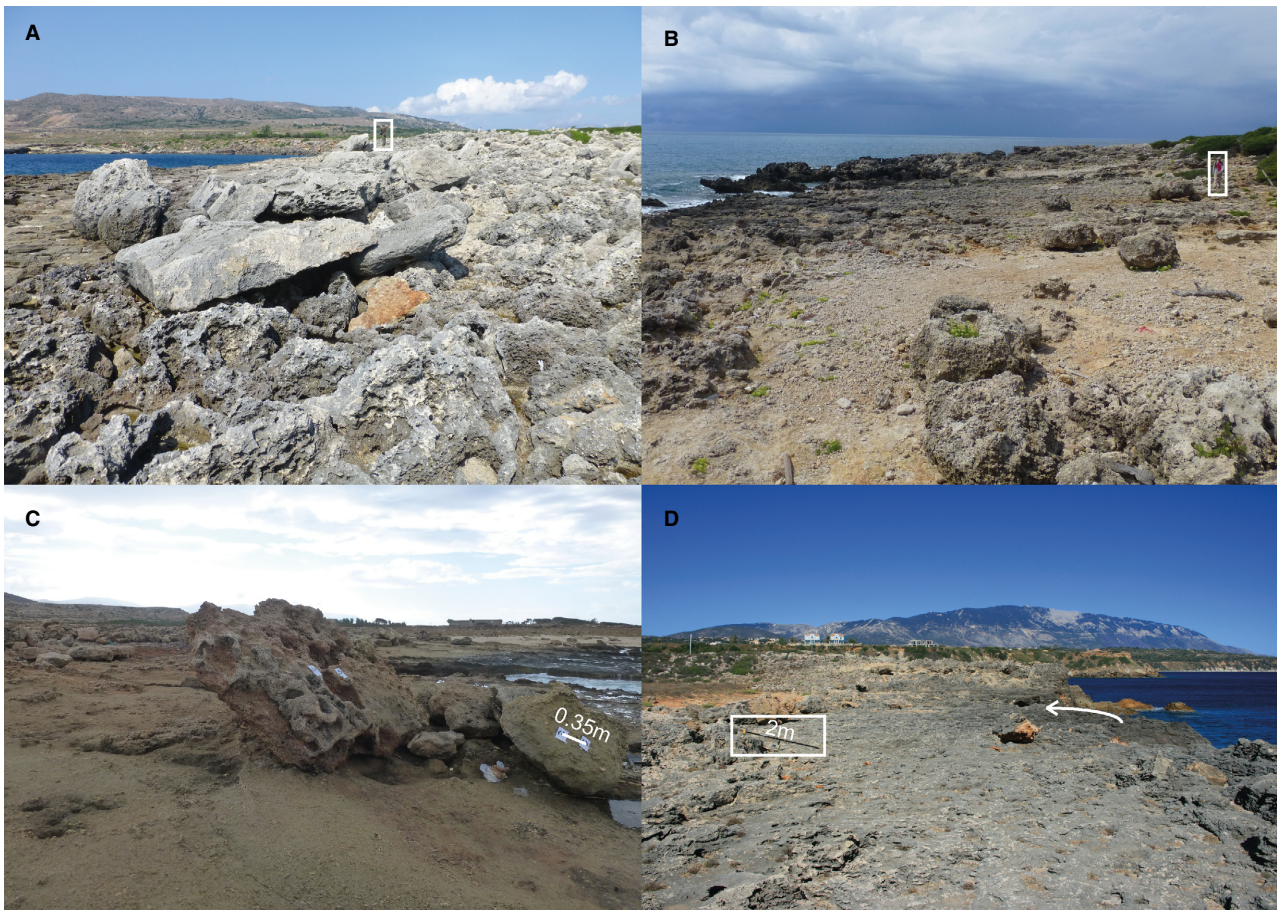


Fig. 2. Photographs of boulders found at different study sites – each with person (*ca* 1.8 m tall) or object for scale. (A) Cape Schinou, Cefalonia. (B) Katakolo, Peloponnese showing a line of boulders parallel to the coast. (C) Cape Skalas, Peloponnese with imbricated boulders close to the shoreline. (D) Cape Ag. Pelagia, Cefalonia showing PEL-ST (a more recently transported boulder) at the cliff edge indicated by white arrow.

present location of the boulders and the shoreline at the moment of boulder displacement, was at least as far as today or even farther (Kraft *et al.*, 1977; Engel *et al.*, 2009; Brückner *et al.*, 2010).

The sites of Gialous Skala and Kaminia Beach on Lefkada Island are characterized by narrow beaches in front of steep inactive cliffs on the windward north-western part of the island. The coastal section at Kaminia Beach is only *ca* 170 m long and the beach is composed of loose cobbles and small boulders up to 50 cm in diameter. The beach section studied at Gialous Skala, is *ca* 500 m long and consists of sand, pebbles and small boulders. Similar to Kaminia Beach, this beach is also flanked by a rocky coast. Towards the south, steep slopes, covered by debris, descend directly into the sea. Both sites show strong annual changes in beach configuration (Hoffmeister *et al.*, 2013).

Study sites near Cape Gerogombos and Cape Schinou are situated on the Paliki Peninsula, Cefalonia Island and represent rocky coastal areas exposed to strong winds and wave dynamics. The two capes are separated by a small embayment, where beachrock-type tsunamites were described by Vött *et al.* (2010). At Cape Gerogombos, large dislocated boulders occur up to several metres above present sea-level (a.p.s.l.) on a cliff-top platform (Hoffmeister *et al.*, 2013). Some of the boulders lie scattered around, others are imbricated and turned upside down. The (supra-)littoral origin of the boulders, is documented by rock pools formed by marine organisms. At Cape Schinou, larger dislocated boulders are lying on a coastal ramp.

Cape Aghia Pelagia is situated in the south of Cefalonia Island, about 8 km south of Argostoli. The site is characterized by a cliff-top platform,

ca 4 m a.p.s.l., in the south-east, and a ramp-type topography in the south-west. The whole site is covered by abundant dislocated boulders, found up to 30 m inland.

Cape Katakolo is located about 12 km west of Pyrgos, at the northern part of the Kyparissian Gulf in the western Greece. Towards the south-west, it is directly exposed to the open Ionian Sea and characterized by a narrow rocky coastline gradually descending to the present-day shore, with numerous dislocated boulders lying up to 30 m inland. In addition, trim lines, where the vegetation is almost completely missing, extend more than 40 m inland and document strong wave activity.

The site of Cape Skalas in southern Lakonia, Peloponnese, is a flat lying coastal section leeward of Elaphonissos Island, with outstanding imbrication trains of dislocated boulders (Scheffers *et al.*, 2008). On-site geoarchaeological findings indicate that relative sea-level was never higher during the Holocene than it is at present (Scheffers *et al.*, 2008).

METHODOLOGY

Surveying methods

Table 1 lists both survey dates and equipment used. In 2008 and from 2009 to 2011, a terrestrial laser scanner system RIEGL LMS Z-420i (referred to as TLS 1) (RIEGL Laser Measurement Systems GmbH, Horn, Austria) was used. This device is based on the ‘time of flight’ method with an accuracy of 6 mm and a range of 2 to 1000 m. In 2014, a more lightweight FARO LS120 laser scanner (referred to as TLS 2) (FARO, Lake Mary, FA, USA) was used, incorporating the phase-shift method, which resulted in a higher accuracy of 3 mm but a smaller maximum range of up to 120 m.

Field research started in 2014 with low-cost UAV-based recording for the ‘structure from motion’ (SFM) approach (Westoby *et al.*, 2012). In 2014, two DJI Phantom UAVs (DJI, Shenzhen, China) were tested. One was equipped with a gimbal-attached GoPro Hero 3+ black edition (GoPro, San Mateo, CA, USA) with a 12 megapixel (MP) sensor and a fisheye lens (UAV 1), the other was equipped with a fixed Canon PowerShot S110 (Canon, Tokyo, Japan), also with a 12 MP sensor (UAV 2). Because the latter showed greater accuracy, it was used in the 2015 field campaign. In 2016, it was replaced by a more modern version of the Phantom 3 Professional (DJI) with a 12.4 MP sensor; this system was also used in 2017 (referred to as UAV 3).

Manual flying at two different heights was conducted (mean height for all sites ca 25 m above ground), resulting in datasets of between 350 and 650 images. Ground resolution for the derived ‘orthophotos’ was 1 cm per pixel and 2 cm per pixel for digital elevation models. The latter were not used in this study, as the original point clouds were used for change detection.

At all sites, the position of a base point and several additional surveying points were established by using real-time kinematic (RTK) positioning (Topcon Hiper Pro; Topcon Corporation, Livermore, CA, USA), with an accuracy of 1 to 2 cm. These base points were marked with metal screws on bedrock outcrops. All base points were measured 500 times to achieve a reasonable mean position in WGS 1984, UTM 34N and showed an absolute error of 10 to 20 cm. In each study area, the base station of the RTK system was set up at exactly the same position every year or the total station (Trimble M3 DR 1”; Sunnyvale, CA, USA) was registered by the previously set base points, resulting in an accuracy of 1 to 2 cm between each survey. Between two and six different scan positions were chosen for each site, depending

Table 1. Year of survey and equipment used for each site (see Fig. 1 for site location), starting from 2008. (1 = TLS 1; 2 = TLS 2; 3 = UAV 1; 4 = UAV 2; 5 = UAV 3).

Site	Abbreviation	2008	2009	2010	2011	2012	2013	2014	2015	2016	2017
Cape Skalas	ELA	1	–	–	–	–	–	2, 3	–	–	5
Katakolo	KAT	–	1	1	1	–	–	3, 4	4	5	5
Ag. Pelagia	AIR	–	1	1	1	–	–	2, 3	–	–	–
Cape Shinou	SHI	–	1	1	1	–	–	2, 3	–	–	–
Gerogombos A	GER-A	–	1	1	1	–	–	2	–	–	–
Gerogombos B	GER-B	–	1	1	1	–	–	2, 3	–	–	–
Gialous Skala	GIA	–	1	1	1	–	–	2	–	–	–
Kaminia Beach	KAM	–	1	1	1	–	–	2	–	–	–

on the size of the study area and the geomorphological setting. Approximately the same scan positions were used every year to obtain comparable datasets. For all UAV-based recordings, as well as for the Faro laserscanner (TLS 2), the described total station was used to measure the ground control points (GCPs) marked by spray paint crosses and the globe-shaped targets of TLS 2.

Agisoft Photoscan Professional (AgiSoft, 2018), was used to establish point clouds from the image sets acquired by the different UAVs. For each dataset, the software was set to a high accuracy for the alignment of the images and the most common parameters for camera lens optimization (focal length, principal point coordinates, radial and tangential distortion coefficients) were used, relying on the georeferencing by GCPs measured in each area by the total station. Typically, an amount of 12 to 16 equally distributed GCPs were used. The mean error of the GCPs is between 16 mm and 21 mm. Further, a high-quality reconstruction for the dense point cloud generation, with an aggressive depth filtering was conducted.

Boulder reconstruction

For accurate reconstruction of boulder volumes, the different scan positions at each site were directly georeferenced and merged. Afterwards, the registration was enhanced by the iterative closest points-algorithm (ICP). Noise and outliers of the final point cloud for each site were manually removed with the help of incorporated filters. Parameters for each boulder, such as the mean length of boulder axes, were measured manually for each boulder based on the georeferenced dataset. Likewise, the distance to the sea (d.t.s.) and the height above present sea-level (a.p.s.l.) were measured from the centre of the boulder to the nearest point of the present-day shoreline. While some authors classify axes based on the length (Pignatelli *et al.*, 2009; Paris

et al., 2010), for this study the *a*-axis was measured as parallel to the coast line, the *b*-axis as perpendicular to the coast line and the *c*-axis as the height of the boulder, which is common practice in other studies (Noormets *et al.*, 2004; Benner *et al.*, 2010; Etienne *et al.*, 2011).

For optimal boulder reconstruction and gap-filling based on the manually extracted point clouds for each boulder, the software Geomagic Studio (now Geomagic Wrap) was used (3D Systems, 2018). In particular, the bottom side of each boulder was automatically filled and afterwards checked in order to achieve accurate polygonal models. Examples are shown in Fig. 3, additional results can be found in Hoffmeister *et al.* (2014). Thus, the shape of each 3D boulder model was extracted and the accurate boulder volume was determined. Density measurements were obtained by applying the principle of *Archimedes*, using hand-sized samples that had been taken from several dislocated boulders in the study areas.

Wave transport equations

Most studies which reconstruct minimal wave heights required to move boulders, utilise the wave transport equations developed by Nott (2003b). However, these equations have been revised by Pignatelli *et al.* (2009), Benner *et al.* (2010) and Nandasena *et al.* (2011). All of these equations require the lengths of the axes of a selected dislocated boulder as parameters. In contrast, several wave transport equations use the mass of a boulder as a direct input parameter (Noormets *et al.*, 2004; Benner *et al.*, 2010; Etienne *et al.*, 2011; Engel & May, 2012). Generally, the equations can be classified based on the pre-transport scenario. In the submerged scenario the boulder lies loosely offshore in the water, whereas in the joint-bounded scenario the boulder is quarried from a seaward edge of a cliff.

The equations presented by Engel & May (2012) include adjustments based on several existing



Fig. 3. Reconstructed 3D models of boulders found at Cape Schinou, Cefalonia as a perspective view.

approaches and use boulder mass as an input. With the calculation of the wave decay curves, this allows for combination with the results of the multi-temporal surveying. In contrast to the above-mentioned approaches, the presumed pre-transport scenario is a joint-bounded boulder scenario (JBBS), which assumes an initial quarrying out of cliff edges and subsequent sliding. This is the most realistic scenario for all sites, and can be expressed in the following equation:

$$H_{t/s} = \frac{m_b \cdot (\cos \theta + \mu \cdot \sin \theta)}{2 \cdot \rho_w \cdot C_L \cdot q \cdot a \cdot b} \quad (1)$$

where, m_b is the mass of the boulder, θ is the average bedrock angle of the pre-transport setting, μ is the coefficient of static friction (0.65), ρ_w is seawater density (1.02 g cm^{-3}), C_L is the coefficient of lift (0.178) and q is an empirical aspect coefficient (0.73) for correction of the area calculated by multiplying axes a and b . The factor 2 in the denominator is for the tsunami case, for the storm case it is 0.5. Thus, for boulder transport, storm wave heights need to be four times larger than tsunami wave heights. All coefficients are taken from Engel & May (2012).

The latter values are compared to wave decay curves derived from the following equation:

$$H_i = \left(\sqrt{H_w - E} - \frac{5 \cdot X_i}{T \cdot \sqrt{g}} \right)^2 \quad (2)$$

where H_i is the height at a certain distance, X_i is reduced by the difference of the estimated wave height H_w and the mean elevation (E). The wave height H_w , in this case, is derived from the maximum tsunami or storm wave height from Eq. 1 for each site. Several authors add settings or scenarios that fit to a specific region or have been observed by eye-witnesses (Barbano *et al.*, 2010; Engel & May, 2012). In the current study, a tsunami scenario with an inundation height of 4 m is added, which matches the results of the numerical simulations in the Gulf of Kyparissia, Peloponnese, by R bke *et al.* (2013). For a storm setting, a greater height at a certain distance ($H_i = 13.6 \text{ m}$) is used (Barbano *et al.*, 2010). The mean of the 20 maximum values of the maximum wave height (12.3 m) and associated wave periods (13 s) between 2008 and 2018 of buoy data (buoys: Zakynthos and Pylos) from the Poseidon network (HCMR, 2018) was used.

The mass of each boulder was determined by a combination of the 3D model-based volume

and density measurement. Three-dimensional model-based calculations of mass were subsequently compared with results derived from conventional approaches, using the length of boulder axes and approximated density values. For the boulders in the area of Cape Skalas, a density of 2.1 g cm^{-3} was used (Scheffers *et al.*, 2008); for the limestone in the area of Cape Gerogombos a density of 2.3 g cm^{-3} was used, as well as 2.5 g cm^{-3} for boulders from Katakolo and Ag. Pelagia. For the latter two areas, no density measurements were conducted.

Comparisons of point clouds

For the change detection between subsequent surveys of a site, the registered and filtered point clouds of the TLS-instruments and the original point clouds of the UAV-surveys were compared. The comparison of subsequent point clouds was conducted, using the Model-to-Model-Cloud-Comparison algorithm (M3C2), implemented in CloudCompare software (CloudCompare, 2018). This algorithm computes the orthogonal distances between two point clouds (Lague *et al.*, 2013). Between automatically selected core points, a 3D surface is interpolated, from which a normal vector is created for each core point. Along these vectors, the distance to the derived surface of the second point cloud is calculated for each core point. All point clouds were sub-sampled with a point spacing of 1 cm and segmented to a comparable area of interest. These final reduced point clouds were used for these comparisons, in order to reduce computation time and data size. The registration error for the M3C2, was set to 50 mm for all computations. For a generalized visualization, the detected significant elevation changes were interpolated to a 10 cm grid size and changes smaller than 5 cm were neglected.

RESULTS

Boulder mass estimations

All parameters from 3D models of the dislocated boulders, as well as mass calculations based on rock density analyses (3D mass) are listed in Table 2. This comprehensive overview consists of boulder parameters from Cape Schinou, Cefalonia (SCI), shown in Fig. 3, as well as previously published parameters for other boulders (Hoffmeister *et al.*, 2013, 2014). Also shown in

Table 2. Volume, density and mass of dislocated boulders by tape-based (axes a, b and c) and the three-dimensional model-based approach.

Boulder – Id	a.p.s.l. [m]	d.t.s. [m]	<i>a</i> -axis, <i>b</i> -axis, <i>c</i> -axis [m]			Calc. vol. [m ³]	Density [g cm ⁻³]	Est. mass [m ³]	3D volume [m ³]	3D mass [t]	Ratio est. to 3D mass [%]	Tsunami wave height Eq. 1 [m]
ELA-B28	0.5	10.9	1.7	0.9	0.4	0.6	2.3	1.4	0.5	1.1	75	1.5
ELA-B29	0.6	9.9	2.0	1.1	0.7	1.5	2.3	3.6	0.6	1.4	39	1.4
ELA-B30	0.6	8.5	2.5	1.2	0.6	1.8	2.2	4.0	0.9	2.1	52	1.4
ELA-B31	0.4	7.8	1.2	0.6	0.5	0.4	2.3	0.8	0.3	0.7	84	2.0
ELA-B32	0.4	2.8	2.0	1.5	0.3	0.9	2.3	2.0	1.3	3.0	148	2.1
ELA-B33	0.5	2.0	1.8	1.9	0.6	2.1	2.4	5.0	1.2	2.9	57	1.9
ELA-B34	0.4	1.7	2.4	1.5	0.6	2.2	2.3	5.0	1.2	2.8	55	1.7
ELA-B35	0.9	3.5	1.9	1.9	0.4	1.4	2.6	3.7	1.1	2.7	74	1.7
ELA-B36	0.9	1.2	1.9	1.0	0.6	1.1	2.4	2.7	0.5	1.1	40	1.2
ELA-B37	0.5	1.3	2.2	1.8	0.6	2.4	2.3	5.5	1.3	3.0	53	1.6
ELA-B38	0.4	0.7	1.7	1.2	0.6	1.2	2.3	2.8	0.7	1.6	58	1.7
ELA-B39	0.4	1.1	2.2	1.7	0.6	2.2	2.2	5.0	1.2	2.7	53	1.5
ELA-B40	0.4	1.3	3.0	1.5	0.8	3.6	2.3	8.4	1.9	4.4	52	2.1
∅	0.5	4.1	2.0	1.4	0.6	1.7	2.3	3.8	1.0	2.3	65	1.7
±	0.2	3.6	0.4	0.4	0.1	0.8	–	1.9	0.4	1.0	27	0.3
KAT-1	3.1	32.7	2.3	1.8	0.9	3.7	2.5	9.3	2.6	6.5	70	3.6
KAT-2	2.8	35.0	2.2	1.4	0.7	2.2	2.5	5.4	1.5	3.8	71	2.8
KAT-3	3.0	34.0	1.7	1.3	0.8	1.8	2.5	4.4	1.3	3.3	75	3.4
KAT-4	2.8	33.5	1.1	0.8	0.8	0.7	2.5	1.8	0.5	1.3	71	3.2
KAT-5	3.0	34.5	1.3	1.3	0.7	1.2	2.5	3.0	1.1	2.8	93	3.7
KAT-6	1.5	21.8	2.5	1.8	0.7	3.2	2.5	7.9	2.1	5.4	68	2.7
KAT-7	1.4	26.4	0.8	1.1	0.9	0.8	2.5	2.0	0.6	1.5	76	3.8
KAT-8	1.4	24.5	1.5	1.3	0.8	1.6	2.5	3.9	1.2	3.0	77	3.5
KAT-9	2.6	33.7	1.4	1.3	1.0	1.8	2.5	4.6	1.1	2.8	60	3.4
KAT-10	2.7	34.7	1.7	1.6	0.8	2.2	2.5	5.4	1.1	2.7	50	2.3
KAT-11	2.9	33.8	1.3	1.7	0.7	1.5	2.5	3.9	0.9	2.3	60	2.4
KAT-12	2.8	33.8	1.7	1.3	0.7	1.5	2.5	3.9	1.3	3.3	86	3.4
KAT-13	3.8	37.6	1.3	1.2	0.5	0.8	2.5	2.0	0.5	1.3	64	1.8
KAT-14	3.5	36.7	1.3	0.8	0.6	0.6	2.5	1.6	0.4	1.0	64	2.2
KAT-15	2.8	35.9	1.6	2.2	0.8	2.8	2.5	7.0	1.4	3.6	51	2.3
KAT-16	3.4	35.4	0.7	1.4	0.6	0.6	2.5	1.5	0.5	1.3	85	2.9
∅	2.7	32.8	1.5	1.4	0.8	1.7	2.5	4.2	1.1	2.9	70	3.0
±	0.7	4.3	0.5	0.4	0.1	0.9	–	2.3	0.6	1.5	12	0.6
PEL-1	4.3	17.9	1.7	1.3	0.7	1.5	2.5	3.9	0.9	2.3	58	2.3
PEL-2	4.0	19.9	2.4	2.0	0.7	3.4	2.5	8.4	2.4	6.0	71	2.8
PEL-3	3.9	15.8	1.8	1.1	1.0	2.0	2.5	5.0	1.8	4.5	91	5.1
PEL-4	3.9	17.2	1.2	0.8	0.5	0.5	2.5	1.2	0.4	1.0	83	2.4
PEL-5	3.9	17.5	1.6	1.4	0.7	1.6	2.5	3.9	0.8	2.0	51	2.0
PEL-6	4.0	18.5	1.8	1.9	0.6	2.1	2.5	5.1	1.4	3.5	68	2.3
PEL-ST	4.2	4.5	2.0	0.9	0.6	1.1	2.5	2.7	0.9	2.3	83	2.8
PEL-7	5.1	16.3	2.2	1.6	0.6	2.1	2.5	5.3	1.3	3.3	62	1.5
PEL-8	4.0	14.0	2.7	1.7	0.8	3.7	2.5	9.2	2.0	5.0	54	1.4
∅	4.1	15.7	1.9	1.4	0.7	2.0	2.5	5.0	1.3	3.3	67	2.8
±	0.4	4.3	0.4	0.4	0.1	1.0	–	2.4	0.6	1.5	13.4	1.0
GER-ST5	3.2	62.4	3.4	3.2	0.9	9.8	2.5	24.7	4.5	11.4	46	2.4
GER-top	1.9	40.3	3.5	2.8	0.9	8.8	2.5	22.2	5.0	12.5	56	2.9
GER-base	2.0	41.5	3.0	2.4	1.0	7.2	2.5	18.1	3.8	9.5	52	3.0

Table 2. (continued)

Boulder – Id	a.p.s.l. [m]	d.t.s. [m]	α -axis, b -axis, c -axis [m]			Calc. vol. [m ³]	Density [g cm ⁻³]	Est. mass [m ³]	3D volume [m ³]	3D mass [t]	Ratio est. to 3D mass [%]	Tsunami wave height Eq. 1 [m]
Ø	2.4	48.1	3.3	2.8	0.9	8.6	2.5	21.7	4.4	11.1	51	2.8
±	0.6	10.1	0.2	0.3	0.0	1.1	–	2.7	0.5	1.2	4	0.3
SCI-1	3.2	11.0	1.7	2.8	0.9	4.3	2.3	9.9	2.9	6.6	67	2.9
SCI-2	1.5	15.0	2.6	1.1	0.9	2.6	2.3	5.9	2.0	4.5	76	3.4
SCI-3	1.5	16.5	1.3	1.3	1.0	1.7	2.3	3.9	1.1	2.4	63	3.1
SCI-4	1.9	28.1	5.3	2.2	1.5	17.5	2.3	40.2	11.1	25.4	63	4.6
SCI-5	2.4	29.3	0.7	0.9	0.6	0.4	2.3	0.9	0.4	0.9	106	3.1
SCI-6	2.2	27.9	0.7	1.6	0.6	0.7	2.3	1.5	0.7	1.5	100	2.9
SCI-7	2.5	27.4	1.0	1.7	0.5	0.9	2.3	2.0	0.9	2.1	108	2.7
SCI-8	1.9	27.9	0.9	1.2	0.7	0.7	2.3	1.6	0.5	1.2	73	2.3
SCI-9	1.9	29.9	1.7	1.1	1.0	1.9	2.3	4.3	1.2	2.8	65	3.2
SCI-10	1.8	28.9	1.4	3.3	0.8	3.8	2.3	8.8	2.8	6.5	74	3.0
SCI-11	3.3	37.9	0.9	0.4	0.6	0.2	2.3	0.5	0.3	0.7	148	4.4
SCI-12	3.3	39.3	0.9	0.7	0.4	0.3	2.3	0.6	0.2	0.6	95	1.9
SCI-13	3.4	40.8	0.9	0.8	0.6	0.4	2.3	1.0	0.2	0.5	51	1.5
SCI-14	1.2	28.0	1.5	2.5	1.0	3.8	2.3	8.6	3.0	6.9	80	3.9
SCI-15	1.2	34.9	0.8	1.5	0.9	1.1	2.3	2.5	1.0	2.4	96	4.2
SCI-16	2.7	36.2	1.8	1.2	1.2	2.6	2.3	6.0	2.0	4.6	77	4.5
SCI-17	3.7	43.7	0.7	0.8	0.5	0.3	2.3	0.6	0.3	0.6	100	2.4
SCI-18	3.7	35.5	0.8	0.8	0.5	0.3	2.3	0.7	0.7	1.7	228	5.6
SCI-19	1.1	26.5	0.7	0.7	0.5	0.2	2.3	0.6	0.2	0.5	90	2.2
SCI-20	1.8	32.3	2.0	0.8	0.4	0.6	2.3	1.5	0.6	1.3	91	1.8
SCI-21	0.4	22.4	3.0	1.7	1.9	9.7	2.3	22.3	5.8	13.4	60	5.6
SCI-22	0.5	25.1	1.9	1.2	1.3	3.0	2.3	6.8	2.2	5.0	74	4.7
SCI-23	1.1	29.1	1.6	1.2	0.6	1.2	2.3	2.6	1.1	2.5	93	2.7
SCI-24	1.4	31.5	2.5	1.3	0.9	2.9	2.3	6.7	3.2	7.3	109	4.8
SCI-25	1.9	31.5	1.3	1.6	0.9	1.9	2.3	4.3	1.5	3.4	78	3.4
SCI-26	0.9	27.0	1.6	1.0	1.0	1.6	2.3	3.7	1.1	2.6	69	3.4
SCI-27	1.4	21.1	2.0	2.8	0.8	4.5	2.3	10.3	3.2	7.5	72	2.8
SCI-28	1.4	28.4	1.8	1.9	1.0	3.4	2.3	7.9	2.3	5.2	66	3.2
SCI-29	1.8	25.9	1.6	0.8	1.0	1.3	2.3	2.9	0.9	2.0	68	3.3
Ø	2.0	28.9	1.6	1.4	0.8	2.5	2.3	5.8	1.8	4.2	88	3.4
±	0.9	7.2	0.9	0.7	0.3	3.4	–	7.9	2.1	4.9	33	1.2
Ø	2.3	25.9	2.1	1.7	0.8	3.3	2.4	8.1	1.9	4.7	68	2.7
±	0.5	5.9	0.5	0.4	0.2	1.4	–	3.4	0.9	2.0	18	0.7

a.p.s.l., above present sea-level; d.t.s., distance to sea; calculated = multiplying the axes; 3D = achieved by 3D analysis; Ø and ± represent mean and standard deviation per site and for all boulders. Table includes data from ELA (Cape Skalas) and GER (Gerogombos) (Hoffmeister *et al.*, 2014), data from PEL (Ag. Pelagia) and KAT (Katakolo) (Hoffmeister *et al.*, 2013), as well as SCI (Cape Schinou).

the table is volume [calculated by multiplying the different axes (calc.)] and the estimated mass [calculated with estimated density values (est.)]. Minimum tsunami wave heights in metres derived from Eq. 1 are also shown. Corresponding minimum storm wave heights are four times larger than tsunami wave heights.

Generally, most values of the 3D model-based masses in Table 2 are considerably smaller than

masses calculated from measurement of boulder axes. As an example, boulders of Cape Schinou, Cefalonia, are presented in Fig. 2. Obviously, the difference is larger for bigger boulders. The 3D model-based masses are generally 12 to 44% smaller than calculations using volumes based on axes calculations and estimated densities, with the greatest difference having been calculated for boulder ELA-B29, which exhibits only

39% of the estimated mass. Several exceptionally large boulders (for example, ELA-B32, KAT-5, PEL-3, SCI-5, SCI-6, SCI-7, SCI-18 and SCI-24) show, as a result of their irregular shapes, nearly similar or larger values (>90%) for the achieved 3D mass, in contrast to their estimated mass. Boulders of Cape Skalas, southern Peloponnese, are located closer to present-day sea-level, as well as at the lowest height above present sea-level, in comparison to all other observed areas. The highest position above present sea-level is observed in boulders from Ag. Pelagia, which are located on a cliff-top platform. The largest boulder (SCI-4) is found at Cape Schinou, Cefalonia Island, with a mass of 25.4 t.

Wave transport equations, decay curves and detected changes

General overview

The results for each boulder and site of the applied wave transport equation are presented in Table 2 and wave decay curves for each boulder site are shown in Fig. 4. Minimum wave heights for storms and tsunamis were derived using Eq. 1 and wave decay curves were derived by applying Eq. 2. For each scenario (setting), two different wave decay curves were computed. One wave decay curve represents the data-driven scenario with the highest wave height of that location derived from Eq. 1. The second curve represents stronger wave scenarios, using the simulated 4 m inundation depth for tsunamis and maximum wave heights, and periods collected from buoy data for the storm scenario. These curves are shown in combination with the derived tsunami and storm wave heights for each boulder at sites depicted in the graphs of Fig. 4. As expected, all calculated wave heights are relatively small compared with other studies, because the boulders are generally smaller.

Based on the extracted wave decay curves shown in Fig. 4, most of the boulders can be further transported from their current position by tsunamis, with the exception of one boulder at Ag. Pelagia and several boulders at Cape Schinou and Katakolo, since these fall below all wave decay curves. In contrast, further transport from their current location is not possible by storm waves for all boulders located at Katakolo and Cape Gerogombos, as well as several boulders at Ag. Pelagia and Cape Schinou, since all of these boulders plot above all calculated curves. All of the boulders at Cape Skalas could be moved by further storm inundation from the current

position. Generally, most of the boulders actually lie in areas which can be reached by storm inundation, except for one boulder lying at a distance of 60 m inland at Cape Gerogombos.

When the current distance from the coast is nil (by virtually moving the boulder position along the x-axis), most of the boulders lie below calculated wave decay curves. Thus, initial quarrying out of the reef edge by both storms and tsunamis, depending on the mass of the boulder, its current position and chosen scenario, is mostly possible. Exceptions are all boulders at Katakolo and Ag. Pelagia and some boulders found at Cape Schinou.

All wave decay curves show the maximum extent of coastal inundation, which fits monitoring results, as the furthest redistribution is detected at the end of each range suggested by the decay curve. Likewise, the end of the non-vegetated spray zone at each site matches with the end of coastal inundation calculated by the wave decay curve of the storm scenarios.

Individual sites

The minimum wave heights calculated for the area of Cape Skalas, Peloponnese (ELA-B28 to ELA-B40) near Elaphonissos Island are the smallest of all generated values (Table 2). This corresponds with the small size of the 13 boulders (Ø 2.3 t) found here. Most of the boulders are imbricated and lie close to the coastline. Although there is evidence of tsunami impact based on fine-grained sediment deposits (Scheffers *et al.*, 2008), the calculated minimum storm wave heights for boulder replacement are very small and storms might be capable of moving these boulders initially from a joint-bounded location (Fig. 4). The calculated minimum wave heights for each boulder are below the line of the wave decay curve generated in the stronger storm scenario and some are even below the line of data-driven calculation. Monitoring results from this site as values of mean difference and areas with significant change are higher, as the boulders of the area which lie closer to the sea are not very elevated. (Table 3). The changes are detectable as sand and gravel redistribution in larger amounts around and beyond the boulders (Fig. 5).

For the time period between 2011 and 2014, Fig. 6A to C shows detailed height changes (in metres) for the following sites: Cape Ag. Pelagia, Cefalonia; Katakolo, Peloponnese; and Cape Schinou, Cefalonia. The 16 boulders at Katakolo, western Peloponnese (Hoffmeister *et al.*,

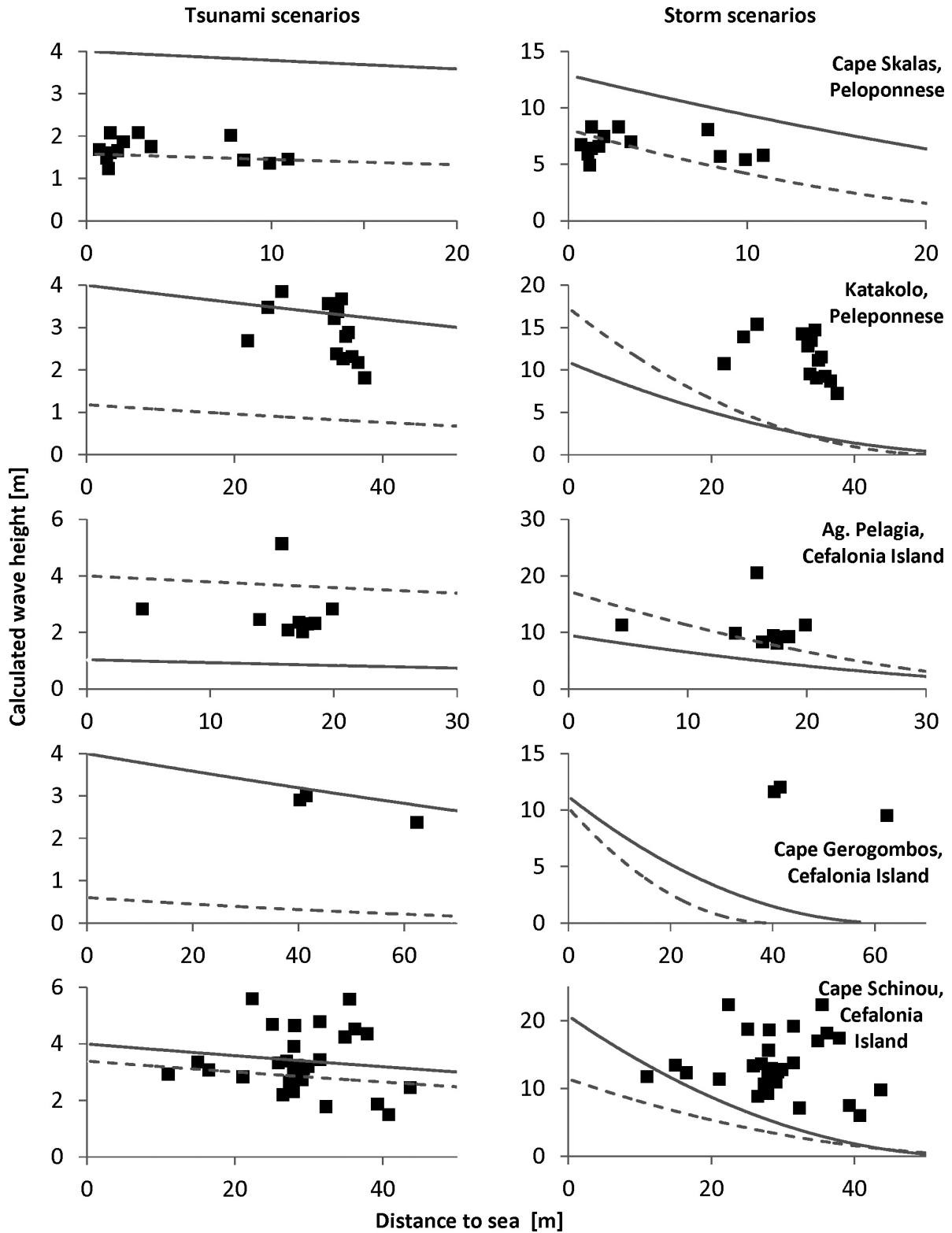


Fig. 4. Graphs for tsunami and storm wave cases at all study sites. The graphs show calculated wave heights (minimum) and the distance to a boulder's (black squares) present-day location. Values were determined from Eq. 1 and wave decay curves from Eq. 2. Both directly derived scenarios based on data (solid lines), as well as estimated, stronger scenarios for the storm and tsunami cases (dashed lines). All values given in metres.

Table 3. Results based on annual comparisons of mean and standard deviation (SD) in metres of the computed height changes by the M3C2 algorithm, as well as the percentage of points with a detected significant difference per site and time interval. Height changes over time are the result of erosion or accumulation. The denoted method [unmanned aerial vehicle (UAV) or terrestrial laser scanning (TLS)], is used for comparison with the prior period; comparisons between both methods are denoted with ‘TLS/UAV’ for the year 2014.

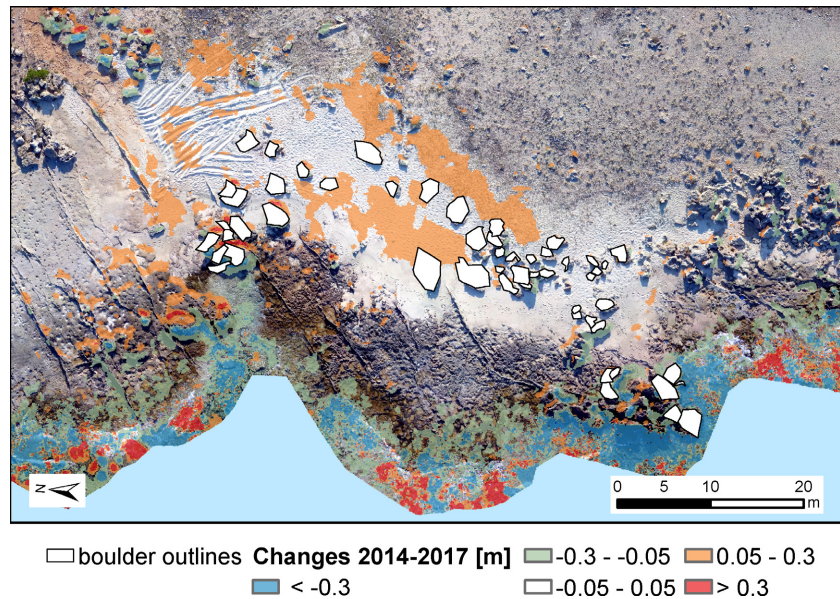
Site	Time period	Mean [m]	Standard deviation [m]	Sig. change [%]
AIR	2010–2009 (TLS)	0.001	0.077	2.67
	2011–2010 (TLS)	0.023	0.088	2.18
	2014–2011 (TLS)	–0.010	0.112	3.96
	2014–2011 (UAV)	–0.017	0.124	10.83
	2014 (TLS/UAV)	–0.001	0.046	0.00
ELA	2014–2008 (TLS)	–0.128	0.273	16.65
	2014–2008 (UAV)	0.109	0.293	6.20
	2017–2014 (TLS)	0.006	0.283	57.10
	2017–2014 (UAV)	0.031	0.095	22.31
GER-A	2010–2009 (TLS)	0.016	0.092	2.60
	2011–2010 (TLS)	–0.009	0.078	2.76
	2014–2011 (TLS)	–0.015	0.108	8.56
GER-B	2010–2009 (TLS)	0.003	0.078	2.48
	2011–2010 (TLS)	0.005	0.107	3.80
	2014–2011 (TLS)	0.002	0.113	5.24
	2014–2011 (UAV)	–0.003	0.116	10.22
	2014 (TLS/UAV)	–0.008	0.104	0.00
GIA	2010–2009 (TLS)	0.049	0.263	55.91
	2011–2010 (TLS)	–0.025	0.279	43.30
	2014–2011 (TLS)	–0.047	0.211	28.14
KAM	2010–2009 (TLS)	–0.122	0.212	25.50
	2011–2010 (TLS)	0.030	0.144	28.00
	2014–2011 (TLS)	–0.094	0.224	27.27
KAT	2010–2009 (TLS)	0.008	0.062	1.28
	2011–2010 (TLS)	0.037	0.082	6.54
	2014–2011 (TLS)	–0.020	0.116	13.66
	2014–2011 (UAV)	–0.018	0.149	17.15
	2014 (TLS/UAV)	0.002	0.113	1.28
	2015–2014 (UAV)	0.038	0.086	13.43
	2016–2015 (UAV)	–0.006	0.096	16.92
	2017–2016 (UAV)	–0.045	0.124	15.94
SCI	2010–2009 (TLS)	0.000	0.084	2.76
	2011–2010 (TLS)	–0.001	0.073	1.88
	2014–2011 (TLS)	0.016	0.108	3.25
	2014–2011 (UAV)	0.005	0.150	16.14
	2014 (TLS/UAV)	0.007	0.111	0.00

2013) are generally larger, lie at a considerably greater distance to the sea (\varnothing 32.8 m) and are more elevated (\varnothing 2.9 m) than the boulders at Cape Skalas. Likewise, boulder mass and corresponding estimated wave heights are greater. Annual monitoring results are shown in Fig. 6B and show significant height changes of approximately 15% of the area per year (Table 3). Most of the dislocated boulders are arranged along a north–south trending line parallel to the trim line, with three exceptions, boulders KAT 6 to

KAT 8. These boulders are located at an edge closer to the sea (\varnothing 25 m). This pattern can be observed in Figs 4 and 5, where two linear groups are distinguishable. As shown in Fig. 6B, redistribution of gravel and sand is detected around and beyond the boulders, which fits the inundation depth of both storm scenarios.

For the area of Ag. Pelagia, Cefalonia Island, nine boulders (see Hoffmeister *et al.*, 2013) (Table 2), are located on a cliff-top platform (\varnothing

Fig. 5. Detailed height changes (m) for the time period from 2014 and 2017 at Cape Skalas, Peloponnes. A digital orthophoto derived from unmanned aerial vehicle (UAV) imagery is in the background. Height changes (in metres) are detected around the boulders and related to the redistribution of gravel and jetsam. Different sea-levels resulted in some miscalculations.



4 m a.p.s.l). Similar to Katakolo, the boulders are lying in a notional north-east/south-west trending line parallel to the south-eastern fringe of the cliff-top platform, *ca* 17 m away from the present shoreline (Fig. 6C). The location of the boulder PEL-ST is exceptional in that it lies much closer to the edge of the cliff-top platform. Moreover, its surface is reddish in colour, indicating that the boulder has recently been broken out of the weathered bedrock and might have been moved during stronger winter storms prior to the first field campaign (Hoffmeister *et al.*, 2013). The required tsunami wave heights are similar to those presented for Katakolo, Peloponnes. Boulder redistribution from their current positions, as depicted in Fig. 4, is possible for most of the boulders, because these are within the range of the stronger tsunami scenario, but not in the range of the calculated tsunami scenario. In contrast, the stronger storm scenario is capable of initiating movement for only some of the boulders. Boulder PEL-3 is unique, because it could not be moved by any of the tsunami and storm scenarios and also an initial quarrying out of the cliff-edge is not possible by all calculated scenarios. Similar to previous presented results, detected changes end after the actual boulder's position (Fig. 6A). As the cliff-top platform is considerably higher than present-day sea-level, significant changes are smaller (<10%; see Table 3) and related mostly to vegetation growth or decline.

Cape Gerogombos on Cefalonia Island has two monitoring sites (GER-A and GER-B; see Table 3) and the boulder study site lies between these two sites (Hoffmeister *et al.*, 2014). Cape Schinou is located in close proximity to these sites (Fig. 1). The largest boulder at all sites in this current study is located at Cape Schinou (SCI-4; 25.4 t). The boulders located at Gerogombos lie furthest inland of all those monitored in this study. Graphs for Gerogombos in Fig. 4 show that tsunami-induced movement is only possible when using the stronger tsunami scenario, whereas storm waves do not reach the boulders in any scenario and are hardly able to initiate transport from the current location. Likewise, initial transport from the cliff-edge is only slightly possible in both storm scenarios and one boulder cannot be reached by inundation in either scenario.

Compared with the other sites, the boulders at Cape Schinou are mostly larger, with the highest estimated wave heights of all sites. According to Fig. 4, many boulders cannot be moved from their current position or their initial position at the cliff edge by either tsunami scenario. Initial cracking and dislocation is only possible for some of the smaller boulders. Storm related movement is possible for the smaller boulders of the site and initial transport from the cliff edge might be possible in both storm scenarios for most of the boulders. These boulders (Fig. 6C) showed no movement during the monitoring period and results are comparable to those from the Ag. Pelagia site.

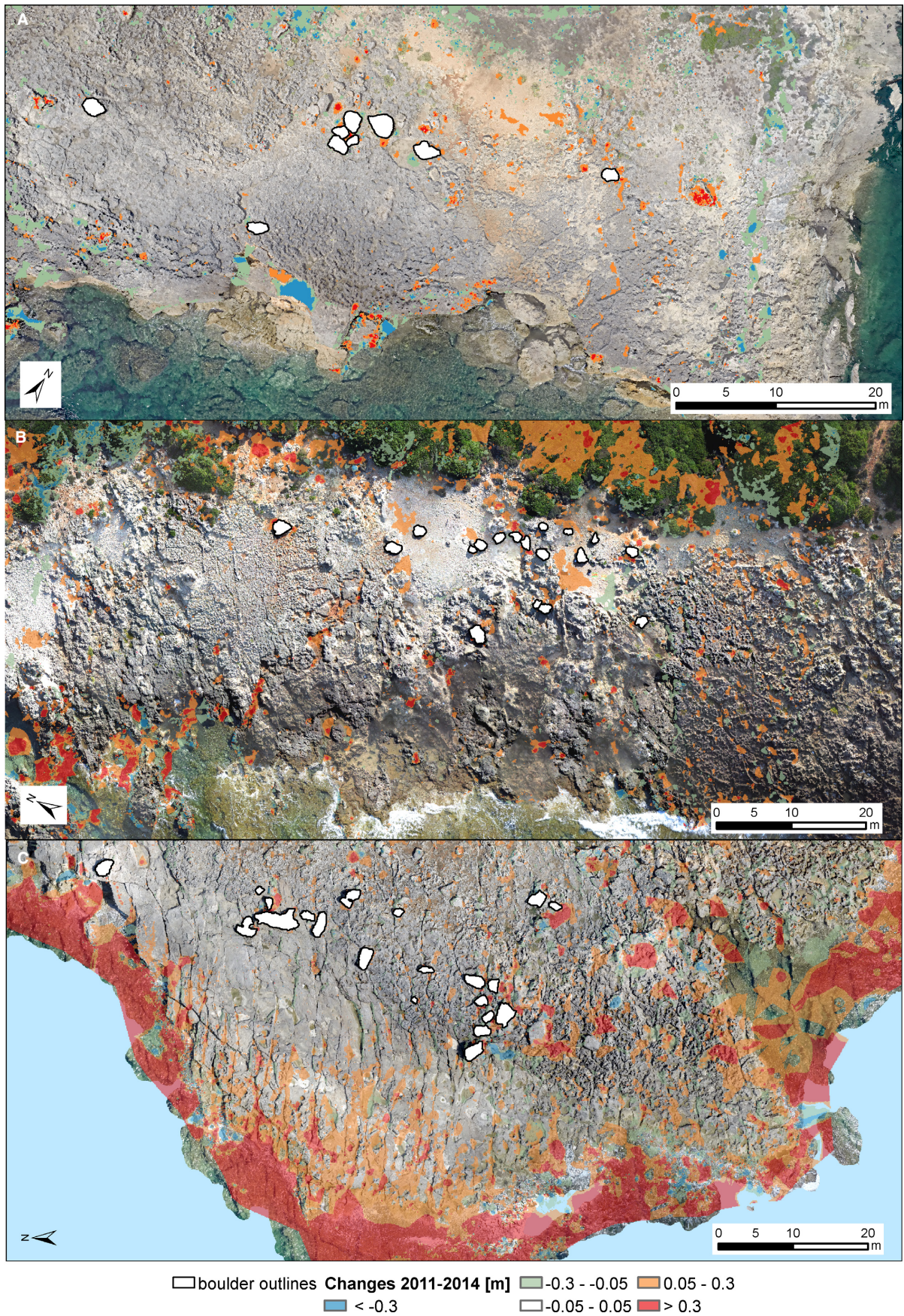


Fig. 6. Detailed height changes (m) for the time period between 2011 and 2014, at Cape Ag. Pelagia, Cefalonia (A), Katakolo, Peloponnes (B) and Cape Schinou, Cefalonia (C). A digital orthophoto, derived from unmanned aerial vehicle (UAV) imagery is in the background. Height changes (in metres) are detected around the boulders and related to the redistribution of gravel and jetsam. Different sea-levels resulted in some miscalculations.

Additional changes

In comparison to the previously presented sites with dislocated boulders, additional sites were monitored to distinguish rare high-energy events from annual changes (Table 3). These sites were monitored since 2009 at different intervals, due to logistical and financial reasons. The annual changes of the sediment budget at the study sites of Kaminia Beach and Gialous Skala are greater (Hoffmeister *et al.*, 2013). The seaweed, sand and gravel is redistributed over a zone that is up to 56% of the whole area. The monitoring sites around Gerogombos, consisting of gravel and pebbles in the spray zone of the elevated terraces show no apparent changes (significant change <10%). Comparison between the TLS and UAV datasets for the year 2014, show average differences smaller than 1 cm and no significant difference is detected.

DISCUSSION

Methodology

The feasibility of the selected monitoring methods for coastal geomorphology was shown to be accurate. Terrestrial laser scanning (TLS) is an appropriate and reliable tool to achieve various parameters of geomorphological features, such as boulders displaced by high-energy waves. For example, Armesto *et al.* (2009) summarized that TLS is of great value for obtaining detailed, highly accurate and rapid non-contact measurements of complex objects. The methods used in this study, show that it is possible to monitor the sediment budget of remote and poorly accessible areas. Within one day of fieldwork, several hundreds of square metres can be observed with high accuracy and resolution. The method is suitable, for an even higher temporal resolution (shorter time periods) depending on organizational matters and logistics. For instance, Pietro *et al.* (2008) successfully used TLS to monitor results following beach nourishment, with monthly surveying of a beach transect, using a set-up similar to that used in the current study. The given accuracy

and resolution of the TLS system is slightly worse than tachymetric profile surveying, but within the range of RTK-DGPS measurements. Because TLS measurements fully cover an area, calculations of volume changes are more accurate than volume calculations from profile surveying (Pietro *et al.*, 2008).

The UAV-based approach for SFM showed similar results to TLS-measurements, as shown by the comparisons in Table 3 for values denoted as '2014 (TLS/UAV)', as mean change, standard deviation and percentage of significant change is close to nil. The smaller detected changes are mostly due to differing perspectives of UAV imagery and occur on the top or the side of larger boulders or channels. Unmanned aerial vehicle (UAV)-based approaches cover larger areas than TLS and thus differences can occur between the datasets. Data acquisition by low-cost drones, as used in this study, is much faster (e.g. Pérez-Alberti & Trenhaile, 2015) and can also be conducted by kites, which eliminates problems related to permits for UAV operation (Autret *et al.*, 2018). Currently, acquisition can be nearly automatic, due to advances in drone technology (for example, following pre-set flight patterns and automated landing with distance sensors). The accuracy in relation to previous TLS-based surveys, relies on the georeference approach and coverage. The GoPro camera was also usable and showed only slight inaccuracies in comparison with the other cameras (for example, reprojection error is 2.3 pixels for the GoPro, 1.4 for the Canon Powershot and 1.3 for the DJI camera). However, after registration and correction, the reported errors are similar, which is again related to the use of many GCPs and a subsequent accurate correction of the different camera models. The data covers the areas in a higher, more equal resolution in terms of point spacing. Computation time, resolution, accuracy and file size depend on camera resolution, flight altitude and overlap. In the previous survey attempts, flight patterns were manually conducted, the overlap is very high and can be decreased for the next surveys by using automated surveying approaches (Eltner *et al.*, 2016). However, acquisition by UAVs can

only be applied under calmer winds and is highly dependent on permits (Casella *et al.*, 2016) which makes TLS-based surveys an important alternative. Likewise, shadowing effects and a very different perspective might hamper coverage at overlapping areas of imbricated boulders. In this case, the site of GER-A was not covered by UAV imagery, due to stronger winds on that specific day in 2014, and the beach sites of Gialous Skala and Kaminia were only recorded by TLS, because people were taking a bath.

A comparison between all datasets of a site is possible, as fixed surveying points were used for georeferencing of data from both methods. This initial registration is important for the comparison between subsequent surveys. In contrast to the previous method of interpolation or triangulation of point clouds for the calculation of high-resolution digital elevation models (DEMs) (Hoffmeister *et al.*, 2013), a direct point cloud comparison by the M3C2-algorithm was applied (Lague *et al.*, 2013). The advantage of this method, according to Lague *et al.* (2013), in contrast to the comparison of DEMs is increased accuracy, in that the local distances between two points along the surface direction are determined, as a result of which changes in the surface orientation or registration errors between two point clouds can also be taken into account and mapped. In addition, the calculation determines a confidence interval that takes into account the roughness, the registration error and the point density and thus checks the statistical significance of the changes measured (Lague *et al.*, 2013). The higher accuracy was also proven by Barnhart & Crosby (2013).

Boulder mass estimations

The TLS-based high-resolution 3D reconstructions of all boulders, in combination with accurate density measurements of large dislocated boulders, yielded more accurate data than previous approaches. Similar results can be found in Spiske *et al.* (2008), Scicchitano *et al.* (2012) and Hoffmann *et al.* (2013). However, the TLS-based method is susceptible to systematic errors (for example, accuracy of TLS), calculation errors (for example, manual 3D reconstruction for areas out of sight) and errors in interpretation (for example, manual determination of boulder axes in the case of complexly shaped boulders). The accuracy can be enhanced, with

more accurate laser scanning devices or detailed photogrammetric approaches (Gienko & Terry, 2014).

Nevertheless, this information is considered to be more realistic and accurate than data achieved by tape measurements. The comparison of 3D model-based volume and density data, with conventional estimations shows lower density values by as much as 22%. Table 2 shows the calculations of volume and mass on the basis of tape measurements of the axes, which results in a mean overestimation of 32% with a 18% variation. Therefore, these results prove that mass estimations of boulders of this size based on simple measurements of the axes, should be multiplied at least by a factor of 0.7. For wave transport equations, which take the mass of a boulder into account (Noormets *et al.*, 2004; Benner *et al.*, 2010; Etienne *et al.*, 2011; Engel & May, 2012), this correction factor should therefore be applied to avoid an overestimation of wave heights and velocities. Likewise, very irregularly shaped boulders (for example, ELA-B31, ELA-B32 and ELA-B33) lead to an underestimation of the mass by multiplying the axes, when a mean axis is taken. Hence, multiplying the axes is not suitable for irregular shaped boulders and a 3D recording approach by TLS or the SFM-approach is preferred.

Boulders and detected changes

Generally, most of the boulders show that minimum tsunami wave heights are within the range of wave heights from the expected tsunami scenarios of this area (1 to 4 m). Minimum wave heights calculated for boulder dislocation at the study sites, correspond to results reported from south-eastern Sicily (Scicchitano *et al.*, 2007; Barbano *et al.*, 2010) and from southern Apulia (Mastronuzzi *et al.*, 2007). Numerical simulations of tsunami wave propagation in the Gulf of Kyparissia, underline the possibility of tsunami wave heights high enough to initiate boulder movement (Tselentis *et al.*, 2010; R bke *et al.*, 2013).

Applying the wave decay curves shows that, for most boulders, storm or tsunami transport from their current position, as well as from a supposed initial position at the cliff edge, is generally possible. However, some boulders lie above all calculated wave decay curves (similar to those in Engel & May, 2012), such as those at Ag. Pelagia and Cape Schinou (Fig. 4). These boulders thus need an even higher initial wave

height of about 6 m for the tsunami case and up to 25 m for the storm case. However, the current location of the boulders might also be the result of several impacts, which would decrease the necessary wave heights for initial and further transport. Likewise, a sliding transport is calculated here. In contrast, a rolling transport would also need decreased initial wave heights, but no evidence of overturning was found. As depicted by the annual comparison, yearly changes occur in the surrounding areas of the boulders (Fig. 6), but no change in the position of the boulders has been detected yet, which proves the applicability of the wave decay curves.

It is assumed that the boulder PEL-ST encountered at Ag. Pelagia, Cefalonia Island, was moved by a winter storm event in 2008/2009 (Hoffmeister *et al.*, 2013) before the first field campaign. This hypothesis is also backed by the buoy data (Fig. 6). This assumption is based on significantly smaller minimum wave heights, with regard to the mass of this boulder and compared to other dislocated boulders. Barbano *et al.* (2010) mentions that boulders were moved during a bigger storm during the 2008/2009 winter season on the Italian side of the Ionian Sea. The boulder PEL-ST is located directly adjacent to a funnel-type, small indentation of the cliff-top rim, which is believed to have enhanced storm-wave influence responsible for boulder dislocation. All of the other dislocated boulders studied near Cape Katakolo and Aghia Pelagia, are arranged in lines and are lying tens of metres inland from the coast, which may indicate that these were transported by a single major inundation (Goto *et al.*, 2011).

Annual changes in the sediment budget of the study sites, are generally negligible to modest (Table 3). This is in good agreement with the analyzed buoy data (Fig. 7), which documents only outstanding storm wave activity for the time period of late 2008 and the beginning of 2009. Most of the sites were initially visited in September 2009. Moreover, the results show that dislocated boulders were not moved at all by winter storm conditions between 2009 and 2017, because the storms do not reach similar maximum wave heights as in the previously described period of 2008/2009 (Fig. 7).

In general, TLS-based and UAV-based SFM derived areal monitoring and 3D models of

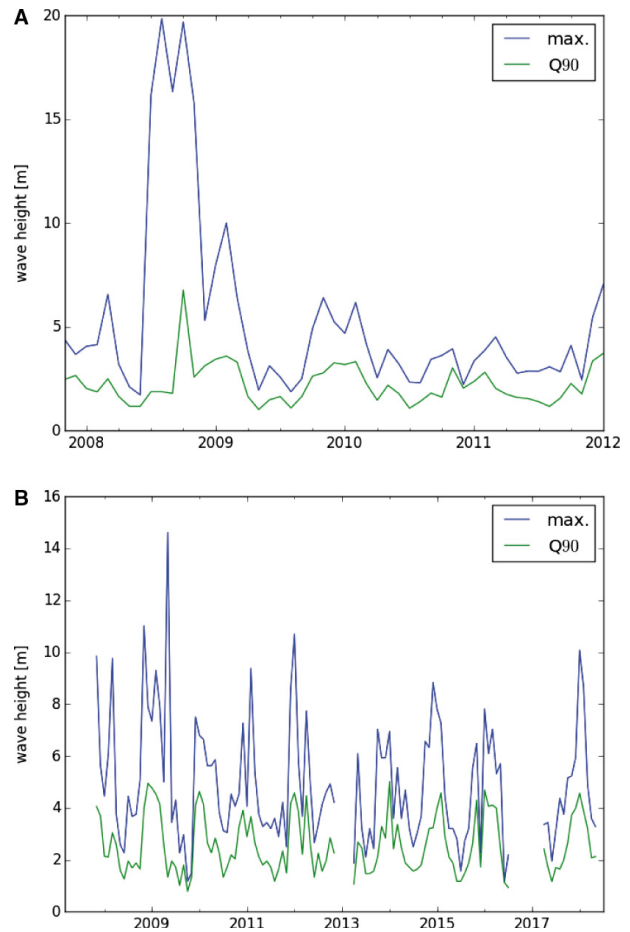


Fig. 7. Maximum wave height data and corresponding 90th percentile (Q90), from the buoys at (A) Zakynthos (ZAK) and (B) Pylos (PYL). Locations are shown in Fig. 1. Please note the difference between the time ranges and wave height scales.

dislocated boulders are considered to offer a reliable method for detecting the effects of changes in the sedimentary budgets, to determine the results of high-energy impacts and to serve as a basis for further hydraulic modelling approaches (Oetjen *et al.*, 2017). Evidence of high-energy impact can only partly be proven, which might also be a consequence of the incorporated wave transport equations. However, for this region and nearby all regarded sites, different kinds of palaeotsunami traces were encountered in near-coast sediment archives (Vött *et al.*, 2010). Finally, numerical simulations of tsunami landfall for the Gulf of Kyparissia (western Peloponnese), including Cape Katakolo, show good agreement between inundation scenarios and field evidence.

CONCLUSIONS

This study provides a comprehensive overview of dislocated boulders in western Greece. The purpose was to examine the distribution, size and mass of these boulders as an input for wave transport equations in comparison to wave decay curves. For the first time, the results of these computations are evaluated with terrestrial laser scanning (TLS) and unmanned aerial vehicle (UAV)-based approaches. Although documented boulders of this area are considerably smaller than boulders reported from other areas, the high seismic and tsunami risk present in western Greece, as well as stronger storms, make this a region of considerable interest for monitoring approaches in order to study high-energy wave impacts on coasts.

This study demonstrates the accuracy of the method used to create 3D models of boulders from TLS. These 3D boulder models are, when compared with manual, tape-based measurements and corresponding calculations of boulder mass and volume, more accurate. Here a mean overestimation of 32% is detected, with a variance of up to 61% depending on boulder shape. In addition, axes-based calculations sometimes underestimate boulder volume and corresponding mass. The parameters of the 3D boulder models derived by TLS, were used in a wave transport equation and wave decay curves in order to distinguish either a possible tsunami-based or storm-based source of dislocation. Initial quarrying of the reef edge, as the chosen pre-transport scenario, is possible by both storms and tsunamis, depending on the mass of the boulder and its current position. A further transport of these boulders from their current position is mostly possible by tsunami waves. For boulders at Cape Skalas and single boulders located at other sites, there might be further movement by storm inundation. However, multiple impacts from storms or tsunamis might decrease the necessary wave heights for boulder transport. Likewise, the necessary wave heights might be even lower, as a sliding transport scenario is regarded here, because no evidence of overturning was found.

Monitoring conducted by TLS and UAV-based approaches worked well and accurately, with fixed survey points re-used for georeferencing tasks. Although the UAV-based approach is much faster, easier and shows better coverage, the presence of strong winds and an absence of local permission for UAV usage can exclude this

method of monitoring. The results of the accurate, direct point cloud comparison in contrast to raster-based comparisons show that, depending on the height above present sea-level, changes occur in different amounts. Most importantly, changes were detected in areas corresponding to the calculated wave decay curves, which includes the surrounding areas of boulders. The boulders exhibited no movement during the observation period. During this time, measured wave heights by buoys were low, but this does not preclude movement as the result of seismically-induced tsunamis and/or stronger storm activity in this region.

ACKNOWLEDGEMENTS

We thank the editors and both anonymous reviewers for improving the contribution. We gratefully acknowledge the financial support of the initial project “Quaternary tsunami events in the eastern Ionian Sea – reconstructing and modelling extreme events based on interdisciplinary geoscientific investigations” (VO 938/3-1) by the German Research Foundation (DFG). Further surveys and investigations were funded by the University of Cologne.

REFERENCES

- AgiSoft** (2018) AgiSoft PhotoScan Professional (version 1.4.2). Available at: <http://www.agisoft.com/downloads/installer/>
- Armesto, J., Ordóñez, C., Alejano, L. and Arias, P.** (2009) Terrestrial laser scanning used to determine the geometry of a granite boulder for stability analysis purposes. *Geomorphology*, **106**, 271–277.
- Autret, R., Dodet, G., Suanez, S., Roudaut, G. and Fichaut, B.** (2018) Long-term variability of supratidal coastal boulder activation in Brittany (France). *Geomorphology*, **304**, 184–200.
- Barbano, M.S., Pirrotta, C. and Gerardi, F.** (2010) Large boulders along the south-eastern Ionian coast of Sicily: storm or tsunami deposits? *Mar. Geol.*, **275**, 140–154.
- Barnhart, T.B. and Crosby, B.T.** (2013) Comparing two methods of surface change detection on an evolving thermokarst using high-temporal-frequency terrestrial laser scanning, Selawik River, Alaska. *Remote Sens.*, **5**, 2813–2837.
- Benner, R., Browne, T., Brückner, H., Kelletat, D. and Scheffers, A.M.** (2010) Boulder transport by waves: progress in physical modeling. *Z. Geomorphol.*, **54**, 127–146.
- Brückner, H., Kelterbaum, D., Marunchak, O., Porotov, A. and Vött, A.** (2010) The Holocene sea level story since 7500 BP – lessons from the Eastern Mediterranean, the Black and the Azov Seas. *Quatern. Int.*, **225**, 160–177.

- Casella, E., Rovere, A., Pedroncini, A., Stark, C.P., Casella, M., Ferrari, M. and Firpo, M. (2016) Drones as tools for monitoring beach topography changes in the Ligurian Sea (NW Mediterranean). *Geo-Mar. Lett.*, **36**, 151–163.
- Clément, C., Hirn, A., Charvis, P., Sachpazi, M. and Marnelis, F. (2000) Seismic structure and the active hellenic subduction in the Ionian islands. *Tectonophysics*, **329**, 141–156.
- CloudCompare (2018) Cloud Compare (version 2.9.1). Available at: <https://www.danielgm.net/cc/>.
- Cox, R., Jahn, K.L., Watkins, O.G. and Cox, P. (2018a) Extraordinary boulder transport by storm waves (west of Ireland, winter 2013–2014), and criteria for analysing coastal boulder deposits. *Earth-Sci. Rev.*, **177**, 623–636.
- Cox, R., Lopes, W.A. and Jahn, K.L. (2018b) Quantitative roundness analysis of coastal boulder deposits. *Mar. Geol.*, **396**, 114–141.
- 3D Systems (2018) Geomagic Wrap (version 2017). Available at: <https://www.3dsystems.com/software/geomagic-wrap>.
- Eltner, A., Kaiser, A., Castillo, C., Rock, G., Neugirg, F., Abellan, A. and Abellán, A. (2016) Image-based surface reconstruction in geomorphometry—merits, limits and developments. *Earth Surf. Dynam.*, **4**, 359–389.
- Engel, M. and May, S.M. (2012) Bonaire's boulder fields revisited: evidence for Holocene tsunami impact on the Leeward Antilles. *Quatern. Sci. Rev.*, **54**, 126–141.
- Engel, M., Knipping, M., Brückner, H., Kiderlen, M. and Kraft, J.C. (2009) Reconstructing middle to late Holocene palaeogeographies of the lower Messenian plain (southwestern Peloponnese, Greece): coastline migration, vegetation history and sea level change. *Palaeogeogr. Palaeoclimatol. Palaeoecol.*, **284**, 257–270.
- Etienne, S., Buckley, M., Paris, R., Nandasena, A.K., Clark, K., Strotz, L., Chagué-Goff, C., Goff, J. and Richmond, B. (2011) The use of boulders for characterising past tsunamis: lessons from the 2004 Indian Ocean and 2009 South Pacific tsunamis. *Earth-Sci. Rev.*, **107**, 76–90.
- Gienko, G.A. and Terry, J.P. (2014) Three-dimensional modeling of coastal boulders using multi-view image measurements. *Earth Surf. Proc. Land.*, **39**, 853–864.
- Goto, K., Miyagi, K., Kawamata, H. and Imamura, F. (2010a) Discrimination of boulders deposited by tsunamis and storm waves at Ishigaki Island, Japan. *Mar. Geol.*, **269**, 34–45.
- Goto, K., Okada, K. and Imamura, F. (2010b) Numerical analysis of boulder transport by the 2004 Indian Ocean tsunami at Pakarang Cape, Thailand. *Mar. Geol.*, **268**, 97–105.
- Goto, K., Miyagi, K., Kawana, T., Takahashi, J. and Imamura, F. (2011) Emplacement and movement of boulders by known storm waves – field evidence from the Okinawa Islands, Japan. *Mar. Geol.*, **283**, 66–78.
- Hellenic Centre for Marine Research (HCMR), 2018. Poseidon Operational Oceanography System. Available at: <http://www.poseidon.hcmr.gr>
- Hoffmann, G., Reicherter, K., Wiatr, T., Grützner, C. and Rausch, T. (2013) Block and boulder accumulations along the coastline between Fins and Sur (Sultanate of Oman): tsunamigenic remains? *Nat. Hazards*, **65**, 851–873.
- Hoffmeister, D., Tilly, N., Curdt, C. and Ntageretzis, K. (2013) Monitoring annual changes of the coastal sedimentary budget in western Greece by terrestrial laser scanning Georg Bareth, Andreas Vött. *Z. Geomorphol. N.F. Suppl. Issue*, **57**, 47–67.
- Hoffmeister, D., Ntageretzis, K., Aasen, H., Curdt, C., Hadler, H., Willershäuser, T., Bareth, G., Brückner, H. and Vött, A. (2014) 3D model-based estimations of volume and mass of high-energy dislocated boulders in coastal areas of Greece by terrestrial laser scanning. *Z. Geomorphol. Suppl. Issues*, **58**, 115–135.
- Imamura, F., Goto, K. and Ohkubo, S. (2008) A numerical model for the transport of a boulder by tsunami. *J. Geophys. Res. Oceans*, **113**, 1–12.
- Kraft, J.C., Aschenbrenner, S.E. and Rapp, G.J. (1977) Paleogeographic reconstructions of coastal aegean archaeological sites. *Science*, **195**, 941–947.
- Lague, D., Brodu, N. and Leroux, J. (2013) Accurate 3D comparison of complex topography with terrestrial laser scanner: application to the Rangitikei canyon (N-Z). *ISPRS J. Photogramm. Remote Sens.*, **82**, 10–26.
- Lau, A., Terry, J.P., Ziegler, A., Pratap, A. and Harris, D. (2018) Boulder emplacement and remobilisation by cyclone and submarine landslide tsunami waves near Suva City, Fiji. *Sed. Geol.*, **364**, 242–257.
- Lorang, M.S. (2011) A wave-competence approach to distinguish between boulder and megaclast deposits due to storm waves versus tsunamis. *Mar. Geol.*, **283**, 90–97.
- Louvari, E., Kiratzi, A.A. and Papazachos, B.C. (1999) The Cephalonia Transform Fault and its extension to western Lefkada Island (Greece). *Tectonophysics*, **308**, 223–236.
- Maouche, S., Morhange, C. and Meghraoui, M. (2009) Large boulder accumulation on the Algerian coast evidence tsunami events in the western Mediterranean. *Mar. Geol.*, **262**, 96–104.
- Marriner, N., Kaniewski, D., Morhange, C., Flaux, C., Giaime, M., Vacchi, M. and Goff, J. (2017) Tsunamis in the geological record: making waves with a cautionary tale from the Mediterranean. *Sci. Adv.*, **3**, 1–13.
- Mastroruzzi, G. and Sansò, P. (2004) Large boulder accumulations by extreme waves along the Adriatic coast of southern Apulia (Italy). *Quatern. Int.*, **120**, 173–184.
- Mastroruzzi, G., Pignatelli, C., Sansò, P. and Selleri, G. (2007) Boulder accumulations produced by the 20th of February, 1743 tsunami along the coast of southeastern Salento (Apulia region, Italy). *Mar. Geol.*, **242**, 191–205.
- May, S.M., Vött, A., Brückner, H. and Smedile, A. (2012) The Gyra washover fan in the Lefkada Lagoon, NW Greece – possible evidence of the 365 AD Crete earthquake and tsunami. *Earth Planets Space*, **64**, 859–874.
- Nandasena, N.A.K., Paris, R. and Tanaka, N. (2011) Reassessment of hydrodynamic equations: minimum flow velocity to initiate boulder transport by high energy events (storms, tsunamis). *Mar. Geol.*, **281**, 70–84.
- Noormets, R., Crook, K.A.W. and Felton, E.A. (2004) Sedimentology of rocky shorelines: 3. Hydrodynamics of megaclast emplacement and transport on a shore platform, Oahu, Hawaii. *Sed. Geol.*, **172**, 41–65.
- Nott, J. (2003a) Tsunami or Storm Waves? -Determining the origin of a spectacular field of wave emplaced boulders using numerical storm surge and wave models and hydrodynamic transport equations. *J. Coast. Res.*, **19**, 348–356.
- Nott, J. (2003b) Waves, coastal boulder deposits and the importance of the pre-transport setting. *Earth Planet. Sci. Lett.*, **210**, 269–276.
- Oetjen, J., Engel, M., Brückner, H., Pudasaini, S.P. and Schüttrumpf, H. (2017) Enhanced field observation based physical and numerical modelling of tsunami induced boulder transport. Phase 1: physical experiments. *Coast. Eng. Proc.*, **1**, 4.
- Papazachos, B.C. and Dimitriu, P.P. (1991) Tsunamis in and near Greece and their relation to the earthquake focal mechanisms. *Nat. Hazards*, **4**, 161–170.

- Paris, R., Fournier, J., Poizot, E., Etienne, S., Morin, J., Lavigne, F. and Wassmer, P. (2010) Boulder and fine sediment transport and deposition by the 2004 tsunami in Lhok Nga (western Banda Aceh, Sumatra, Indonesia): a coupled offshore-onshore model. *Mar. Geol.*, **268**, 43–54.
- Paris, R., Naylor, L.A. and Stephenson, W.J. (2011) Boulders as a signature of storms on rock coasts. *Mar. Geol.*, **283**, 1–11.
- Pérez-Alberti, A. and Trenhaile, A.S. (2015) An initial evaluation of drone-based monitoring of boulder beaches in Galicia, north-western Spain. *Earth Surf. Proc. Land.*, **40**, 105–111.
- Pietro, L.S., O’Neal, M.A. and Puleo, J.A. (2008) Developing Terrestrial-LiDAR-based digital elevation models for monitoring beach nourishment performance. *J. Coast. Res.*, **24**, 1555–1564.
- Pignatelli, C., Sansò, P. and Mastronuzzi, G. (2009) Evaluation of tsunami flooding using geomorphologic evidence. *Mar. Geol.*, **260**, 6–18.
- Rixhon, G., Matthias, S., Engel, M., Mechernich, S., Schroeder-ritzrau, A., Frank, N., Fohlmeister, J., Boulvain, F. and Dunai, T. (2017) Multiple dating approach (14 C, 230 Th/U and 36 Cl) of tsunami-transported reef-top boulders on Bonaire (Leeward Antilles) – current achievements and challenges. *Mar. Geol.*, **396**, 100–113.
- Röbke, B.R., Schüttrumpf, H., Wöfler, T., Fischer, P., Hadler, H., Ntageretzi, K., Willershäuser, T. and Vött, A. (2013) Tsunami inundation scenarios for the Gulf of Kyparissia (western Peloponnese, Greece) derived from numerical simulation and geo-scientific field evidence. *Z. Geomorphol. N.F. Suppl. Issue*, **57/4**, 69–104.
- Rovere, A., Casella, E., Harris, D.L., Lorscheid, T., Nandasena, N.A.K., Dyer, B., Sandstrom, M.R., Stocchi, P., D’Andrea, W.J. and Raymo, M.E. (2017) Giant boulders and Last Interglacial storm intensity in the North Atlantic. *Proc. Natl Acad. Sci.*, **114**, 201712433.
- Sachpazi, M., Hirn, A., Clément, C., Haslinger, F., Laigle, M., Kissling, E., Charvis, P., Hello, Y., Lépine, J.C., Sapin, M. and Ansoerge, J. (2000) Western Hellenic subduction and Cephalonia Transform: local earthquakes and plate transport and strain. *Tectonophysics*, **319**, 301–319.
- Scheffers, A. and Kelletat, D. (2003) Sedimentologic and geomorphologic tsunami imprints worldwide – a review. *Earth-Sci. Rev.*, **63**, 83–92.
- Scheffers, A., Kelletat, D., Vött, A., May, S.M. and Scheffers, S. (2008) Late Holocene tsunami traces on the western and southern coastlines of the Peloponnese (Greece). *Earth Planet. Sci. Lett.*, **269**, 271–279.
- Scicchitano, G., Monaco, C. and Tortorici, L. (2007) Large boulder deposits by tsunami waves along the Ionian coast of south-eastern Sicily (Italy). *Mar. Geol.*, **238**, 75–91.
- Scicchitano, G., Pignatelli, C., Spampinato, C.R., Piscitelli, A., Milella, M., Monaco, C. and Mastronuzzi, G. (2012) Terrestrial Laser Scanner techniques in the assessment of tsunami impact on the Maddalena peninsula (south-eastern Sicily, Italy). *Earth Planets Space*, **64**, 889–903.
- Shah-hosseini, M., Morhange, C., Naderi Beni, A., Marriner, N., Lahijani, H., Hamzeh, M. and Sabatier, F. (2011) Coastal boulders as evidence for high-energy waves on the Iranian coast of Makran. *Mar. Geol.*, **290**, 17–28.
- Shah-Hosseini, M., Saleem, A., Mahmoud, A.M.A. and Morhange, C. (2016) Coastal boulder deposits attesting to large wave impacts on the Mediterranean coast of Egypt. *Nat. Hazards*, **83**, 849–865.
- Soloviev, S.L., Solovieva, O.N., Go, C.N., Kim, K.S. and Shchetnikov, N.A. (2000) Tsunamis in the Mediterranean Sea 2000 B.C.-2000. In: *Advances in Natural and Technological Hazards Research*, Springer. <https://www.springer.com/gp/book/9780792365488>
- Spiske, M., Böröcz, Z. and Bahlburg, H. (2008) The role of porosity in discriminating between tsunami and hurricane emplacement of boulders – a case study from the Lesser Antilles, southern Caribbean. *Earth Planet. Sci. Lett.*, **268**, 384–396.
- Switzer, A.D. and Burston, J.M. (2010) Competing mechanisms for boulder deposition on the southeast Australian coast. *Geomorphology*, **114**, 42–54.
- Terry, J.P., Lau, A.Y.A. and Etienne, S. (2013) *Reef-Platform Coral Boulders*. Springer, Singapore city, Singapore.
- Tselentis, G.A., Stavrakakis, G., Sokos, E., Gkika, F. and Serpetsidaki, A. (2010) Tsunami hazard assessment in the Ionian Sea due to potential tsunamogenic sources – results from numerical simulations. *Nat. Hazards Earth Syst. Sci.*, **10**, 1021–1030.
- Vacchi, M., Rovere, A., Zouros, N. and Firpo, M. (2012) Assessing enigmatic boulder deposits in NE Aegean Sea: importance of historical sources as tool to support hydrodynamic equations. *Nat. Hazards Earth Syst. Sci.*, **12**, 1109–1118.
- Vött, A., Bareth, G., Brückner, H., Curdt, C., Fountoulis, I., Grapmayer, R., Hadler, H., Hoffmeister, D., Klasen, N., Lang, F., Masberg, P., May, S.M., Ntageretzi, K., Sakellariou, D. and Willershäuser, T. (2010) Beachrock-type calcarenitic tsunamites along the shores of the eastern Ionian Sea (western Greece) – case studies from Akarnania, the Ionian Islands and the western Peloponnese. *Z. Geomorphol.*, **54**, 1–50.
- Westoby, M.J., Brasington, J., Glasser, N.F., Hambrey, M.J. and Reynolds, J.M. (2012) “Structure-from-Motion” photogrammetry: a low-cost, effective tool for geoscience applications. *Geomorphology*, **179**, 300–314.

Manuscript received 31 July 2018; revision accepted 19 February 2020